Journal of Materials Chemistry A

A Combined SECM and Electrochemical AFM Approach to Probe Interfacial Processes Affecting Molecular Reactivity at Redox Flow Battery Electrodes

Journal:	*Journal of Materials Chemistry A*
Manuscript ID	TA-ART-01-2020-000836.R1
Article Type:	Paper
Date Submitted by the Author:	27-Feb-2020
Complete List of Authors:	Watkins, Tylan; Sandia National Laboratories Sarbapalli, Dipobrato; University of Illinois at Urbana-Champaign, Chemistry Counihan, Michael; University of Illinois at Urbana-Champaign, Chemistry Danis, Andrew; University of Illinois at Urbana-Champaign, Chemistry Zhang, Jingjing; Argonne National Laboratory, Chemical Sciences and Engineering Zhang, Lu; Argonne National Laboratory, Chemical Science & Engineering Zavadil, Kevin; Sandia National Laboratories, Material, Physical and Chemical Sciences Rodriguez-Lopez, Joaquin; University of Illinois at Urbana-Champaign, Chemistry

A Combined SECM and Electrochemical AFM Approach to Probe Interfacial Processes Affecting Molecular Reactivity at Redox Flow Battery Electrodes

Tylan Watkins,[†,a,d] Dipobrato Sarbapalli,[†,b,d] Michael J. Counihan,[†,b,d] Andrew S. Danis,[b,d] Jingjing Zhang,[c,d] Lu Zhang,[c,d] Kevin R. Zavadil,[a,d,*] Joaquín Rodríguez-López[b,d,*]

[a] Material, Physical and Chemical Sciences Center, Sandia National Laboratories, Albuquerque, NM 87185, USA

[b] Department of Chemistry, University of Illinois at Urbana-Champaign, 600 South Mathews Avenue, Urbana, IL 61801, USA

[c] Chemical Sciences and Engineering Division, Argonne National Laboratory, 9700 South Cass Avenue, Argonne, IL 60439, USA

[d] Joint Center for Energy Storage Research, Argonne, IL 60439, USA

Abstract

Redox flow batteries are attractive technologies for grid energy storage since they use solutions of redox-active molecules that enable a superior scalability and the decoupling of power and energy density. However, the reaction mechanisms of the redox active components at RFB electrodes are complex, and there is currently a pressing need to understand how interfacial processes impact the kinetics and operational reversibility of RFB systems. Here, we developed a combined electrochemical imaging methodology rooted in scanning electrochemical microscopy (SECM) and atomic force microscopy (AFM) for exploring the impact of electrode structure and conditioning on the electron transfer properties of model redox-active dialkoxybenzene derivatives, 2,5-di-*tert*-butyl-1,4-bis(2-methoxyethoxy)benzene (C1) and 2,3-dimethyl-1,4-dialkoxybenzene (C7). Using AFM and secondary-ion mass spectrometry (SIMS), we observed the formation of interfacial films with distinct mechanical properties compared to those of cleaved graphitic surfaces, and exclusively during reduction of electrogenerated radical cations. These films had an impact on the median rate and distribution of the electron transfer rate constant at the basal plane of multilayer and single layer graphene electrodes, displaying kinetically-limited values that did not yield the activation expected per the Butler-Volmer model with a transfer coefficient ~0.5. These changes were dependent on redoxmer structure: SECM showed strong attenuation of C7 kinetics by a surface layer on MLG and SLG, while C1 kinetics were only affected by SLG. SECM and AFM results together show that these limiting films operate exclusively on the basal plane of graphite, with the edge plane showing a relative insensitivity to cycling and operation potential. This integrated electrochemical imaging methodology creates new opportunities to understand the unique role of interfacial processes on the heterogeneous reactivity of redoxmers at electrodes for RFBs, with a future role in elucidating phenomena at high active concentrations and spatiotemporal variations in electrode dynamics.

Introduction

Redox flow batteries (RFBs) are a promising technology for integrating renewable energy sources into the electrical grid at a large scale.[1,2] In a RFB, soluble redox-active species (i.e. *redoxmers*) placed in a flow field engage in electron transfer (ET) reactions with current collectors, typically made out of carbon.[3] Graphitic carbons are one of the more cost-effective materials for redox flow battery electrodes, an essential aspect of scalability in these systems;[4,5] therefore, we are motivated to understand the reactivity of the various features of graphitic electrodes towards redoxmers. Ideally, reactions with redoxmers only involve outer-sphere ET via electron tunneling to and from the electrode, observations of higher chemical and electrochemical complexity are pervasive in the field. These range from a strong sensitivity of ET kinetics to the presence of surface functional groups,[6] to the concentration of electrolyte and the redox active components,[7] and the charge-mediating properties of adsorbed redoxmer films,[8] and are further exacerbated by homogeneous reaction mechanisms.[9,10,11] Consequently, there is a pressing need to develop methodologies that address these complicating factors, especially in emerging technologies[12,13] such as non-aqueous redox flow batteries (NRFBs). NRFBs maximize the potential of the synthetic organic toolbox for molecular design[10,11] and device engineering[14,15,16] by utilizing organic solvents to access higher redox potential active species, thus increasing the battery's energy density.[17] However, in comparison to aqueous technologies, NRFBs are incipient, and the interfacial reaction mechanisms underpinning the high redox potential redoxmers used in them remain largely unexplored. Understanding these mechanisms could provide additional insight to improve the efficiency of NRFBs[18,19,20] through identifying processes that hinder heterogeneous electron transfer (ET).

Film formation at the electrode/electrolyte interface is a common factor impacting ET since it results from several mechanisms, including precipitation driven by solute solubility,[21] interactions between electrolyte and redox components,[22] adsorption due to π–π stacking,[23,24] or complex homogeneous mechanisms occurring in the diffusion layer.[25] These mechanisms depend on the chemistry of the catholyte or anolyte, the positive- and negative-side redox couples, respectively, that store charge in RFBs. For example, in a recent study of dialkoxybenzene (DAB) catholytes, it was observed that sterically protected molecules were able to cycle longer in RFBs than asymmetric, less-protected analogues.[26] The degradation of 2,3-dimethyl-1,4-dialkoxybenzene (also called C7) radical cations was proposed via a dimerization pathway where subsequent homogeneous reactions generated a dimer species (Scheme 1), which was argued as responsible for the decay of the coulombic efficiency over time.[26,27] We postulate that in addition to deleterious homogeneous reactions, reactions occurring at the electrode surface also influence the battery lifetime in this system and other NRFBs. These heterogeneous processes may include assisting dimerization reactions, catalyzing catholyte or electrolyte decomposition to form blocking films, or a combination of mechanisms (Scheme 1).

Herein, we establish a first step towards detecting changes in the ET rate constant for model DAB redoxmers as a function of electrode potential cycling history, electrode structure, and (preliminarily) electrolyte composition. We introduce scanning electrochemical microscopy (SECM) methodology to characterize spatiotemporally-resolved changes in the electron transfer (ET) behavior during electrode operation. In contrast to previous SECM studies of film and interphase formation on lithium-ion type systems, including those regarding cathodic or anodic

solid-electrolytes and those using DAB species as innocent mediators,[28,29,30,31,32] we are concerned with changes in the chemistry and electrochemistry of DAB redoxmers themselves at pristine carbon interfaces, as this is the relevant case for their use in RFBs. Complementing SECM, *in situ* atomic force microscopy (AFM) provides evidence about the formation of interfacial nano-structures that impact, and ultimately control, the ET process. To unravel interfacial mechanisms in the DAB catholyte class, C1 (2,5-di-*tert*-butyl-1,4-bis(2-methoxyethoxy)benzene, also known as DBBB)[33] and C7 were compared due to their steric differences and proven cycling efficiencies (Scheme 2).[26,27] Highly ordered pyrolytic graphite (HOPG) and single- and multilayer graphene (SLG, MLG) were used as model graphitic electrodes that enabled probing the reactivity of relevant surface structural motifs.[34,35,36] The complementarity of these two scanning probe techniques to diagnose electrode health in relation to mechanical and morphological changes at the interface will create new opportunities to understand what is (and what is not) consequential to cycle and/or shelf life in NRFB systems.

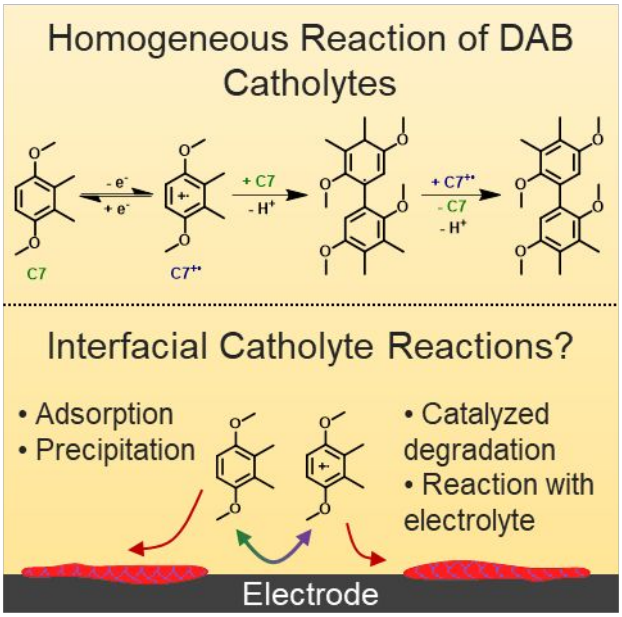

Scheme 1. *Decomposition of Dialkoxybenzene (DAB) Catholytes*. (A) The dimerization of charged DAB molecules via homogeneous reaction as proposed in Ref. 24. (B) The role of the electrode in interfacial degradation has not been thoroughly explored.

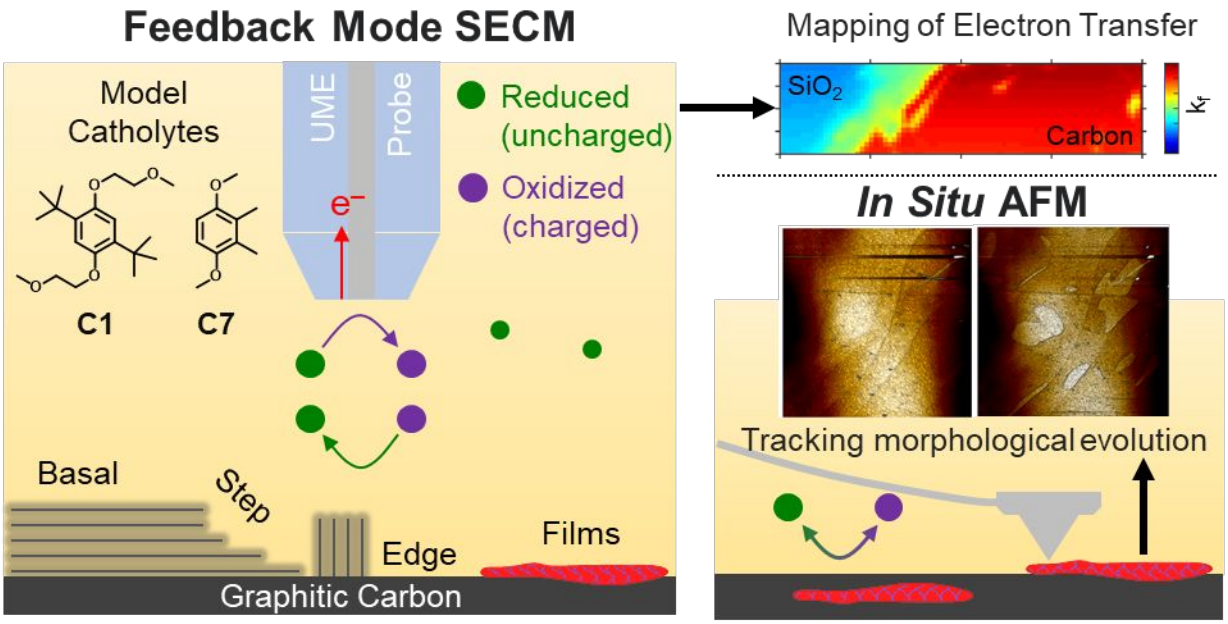

Scheme 2. *Interrogating Electrode Degradation during Catholyte Cycling*. (Left, Top Right) SECM in the feedback mode was used to quantify changes in ET kinetics between different graphitic electrode structures and during cycling over time. (Bottom Right) *In situ* AFM was used to map morphological changes at the interface during catholyte cycling.

Materials and Methods

Materials

All chemicals were purchased from commercial sources and used as received. Propylene carbonate (PC, anhydrous, 99.7%), lithium tetrafluoroborate ($LiBF_4$, ≥98%), ferrocene (98%), $Li_4Ti_5O_{12}$ (LTO, >99% Sigma Aldrich), and $LiFePO_4$ (LFP, >97%) were purchased from Sigma-Aldrich. Lithium bis(trifluoromethanesulfonyl)imide (LiTFSI, 99.99%) was purchased from Ossila. Polyvinylidene fluoride (PVDF, High Purity) was purchased from Solvay. Ketjen black (KB, <30 ppm metal impurity) was purchased from Alibaba. Propylene carbonate was used as the solvent here due to its low volatility in such a way that electrolyte and redoxmer concentrations during SECM and AFM testing were consistent over many hours of testing. C1 and C7 were synthesized via previously established procedures.[26,27]

Multilayer graphene (MLG) was synthesized in house via chemical vapor deposition; details can be found in the Supporting Information (Section 1B). Single layer graphene (SLG) was purchased from GrollTex. Transfer of graphene onto SiO_2-coated Si wafers and characterization of samples by Raman, transmittance, and SEM can be found in the SI. Highly oriented pyrolytic graphite (HOPG, brand grade SPI-2, SPI) and solid slabs of flexible low-density polyethylene (LDPE, 12" x 12" x 1/4"sheet, McMaster-Carr) were used for edge plane HOPG preparation, following previous work;[37] more details can also be found in the SI.

Scanning Electrochemical Microscopy

All SECM experiments were performed with CHI-920D scanning electrochemical microscope inside of an argon-filled glovebox (O_2 < 0.1 ppm, H_2O < 0.1 ppm) with substrates mounted in a custom Teflon cell. An ultramicroelectrode probe (UME) with a platinum wire electrode (radius of ca. 2 μm) sealed in patch clamp glass was brought within 2 μm (L ~ 1) of the substrate surface using the catholyte as a redox mediator. A 0.5 mm platinum wire and 1 mm silver wire were used as counter and quasi-reference electrode, respectively. All electrochemical potentials are reported as reference to the Fc/Fc^+ couple in this electrolyte.

For redox imaging, the feedback mode of SECM was employed, in which the redox mediator was oxidized at the probe and re-reduced at the substrate electrode. This redox recycling near the substrate electrode is known as positive feedback and leads to increased currents at the probe (Scheme 2). At a set probe-substrate distance, the current levels depend on the electron transfer rate of the carbon to the oxidized catholyte,[38] so differences in rates due to substrate heterogeneity will appear as higher or lower currents at the probe. Mass transfer limitations at the high current end (*positive feedback,* PF) and at the low current end (*negative feedback,* NF) provide an upper and lower bound for the rate constants that are measured; these bounds in all experimental results are indicated with green and red lines for PF and NF, respectively. All SECM images are presented as the probe current at each pixel, i, normalized to the probe current at semi-infinite distance from the substrate, i_∞, i.e. in the bulk solution.

The nature of the electrode sample here is important in the calculation of kinetic rates. We used samples of single- or multilayer graphene (SLG and MLG) on SiO_2-coated Si wafers, or HOPG sheets insulated in LDPE so that the sample exposed to solution was partially carbon (i.e., a conductor) and partially insulator (Figure S3). This allows approach of the SECM probe to the insulator, leading to NF that does not depend on the kinetics of the mediator, so the exact distance from the substrate is known in each trial. A part of each SECM image always contained some insulator to ensure correct calibration of the probe-substrate distance for kinetic calculations.

Another important aspect of this sample geometry is the ability to perform open circuit (OCP) feedback measurements.[39,40,41] Since the probe electrode is orders of magnitude smaller than the substrate, only a fraction of substrate is impinged with charged catholyte during the imaging. When biased, electrons are forced through the circuit to reduce the $DAB^{\bullet+}$. However, at open circuit, an electron from a DAB or other species outside the probe range can be spontaneously transferred, conducted through the carbon, and given to a $DAB^{\bullet+}$ at the substrate underneath the probe due to the potential difference between the two regions of the conductor, much like a bipolar electrode.[42] The kinetic rates calculated from OCP feedback estimate the innate ability of the electrode to perform electron transfer, and these values are more indicative of changes compared to an external substrate bias generating a mass transfer-limited potential to reduce $DAB^{\bullet+}$. Thus, OCP imaging is more sensitive to changes in substrate behavior, as blocking films hinder not only the ability to re-reduce $DAB^{\bullet+}$ underneath the probe but also the electrode's ability to transfer electrons everywhere in solution. OCP images only are shown here; the corresponding images biased at high overpotential can be found in the SI.

In situ Atomic Force Microscopy

In situ AFM was conducted using a Bruker Dimension Fast Scan Microscope housed in an argon-filled glovebox (O_2 < 1 ppm, H_2O < 1 ppm). Imaging was conducted with ScanAsyst Fluid+ probes operated in Peak Force Tapping mode at a force setpoint between 200 and 600 pN, where variation is driven by differences in cantilever properties. Low force measurements are essential to minimize disruption of any surface films that form. HOPG crystals and graphene films were sealed with an O-ring in a bathtub style cell (430 μL of electrolyte) equipped with $Li_4Ti_5O_{12}$ (LTO)- and $LiFePO_4$ (LFP)-coated Pt wires as counter and reference electrodes, respectively. Each active material in the counter and reference electrodes comprised 50 wt% of a composite with other constituents being 10 wt% PVDF and 40 wt% Ketjen black conductive carbon. LFP was pre-activated with cycling in the electrolyte prior to initiating the imaging experiments. HOPG crystals (grade ZYB, SPI Supplies) were tape cleaved within the glove box just prior the imaging experiment.

Secondary Ion Mass Spectrometry

SIMS analysis was performed on an ION-TOF TOF-SIMS.5 system using a Bi_3^{2+} cluster to obtain both surface spectra and imaging. Images represent spatially correlated secondary ion emission determined by multivariate analysis of all spectra at all pixels.[43] The working electrodes were extracted from the cell, rinsed in dimethylcarbonate (anhydrous, ≥99%, Sigma-Aldrich), and allowed to dry in the glove box. Electrodes were transferred from glove box to SIMS spectrometer under Ar using a sealed transfer pod that prevents air exposure.

Results and Discussion

We explored three NRFB components that may contribute to interfacial degradation: the chemical structure of the catholyte, the structure of the electrode, and the composition of the supporting electrolyte. Since molecule symmetry and sterics were shown to impact bulk behavior,[26,27] we explored this aspect first by comparing the behaviors of C1 and C7 (Scheme 2).

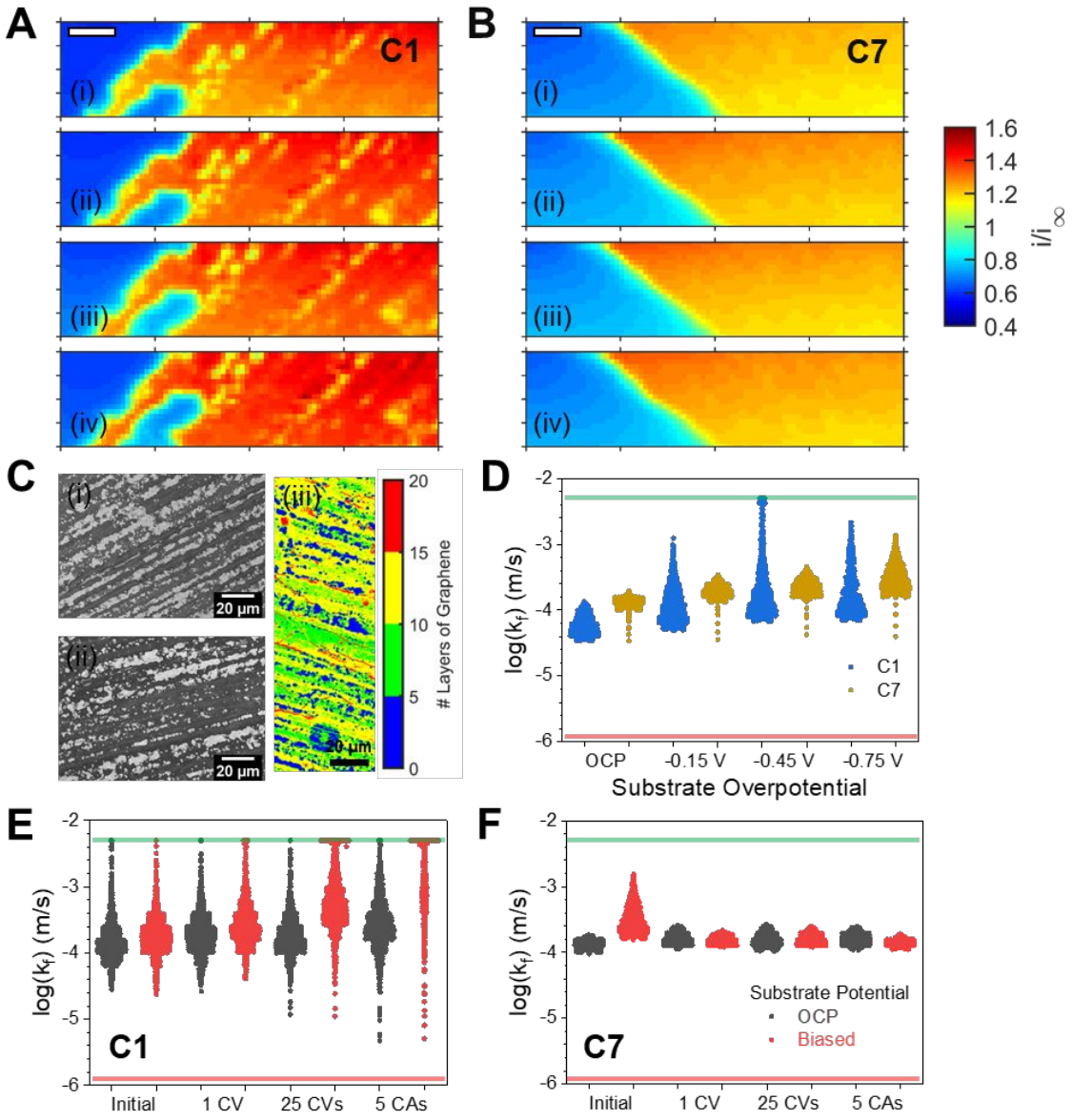

Figure 1. *SECM of C1 and C7 on MLG Substrates*. Normalized SECM images of an MLG electrode at open circuit with 5 mM (A) C1 and (B) C7 as catholyte mediator in $LiBF_4$ electrolyte; image scale bars are 20 μm. Images were taken with the substrate electrode: (i) at the initial condition before substrate biasing, (ii) after 1 substrate CV, (iii) after 25 more substrate CVs, and (iv) after 5 sets of oxidative then reductive chronoamperograms (see SI for more information). (C) SEM images of MLG substrates used for (i) C1 and (ii) C7 imaging. UV-Vis transmittance imaging (iii) reveals the graphitic layer number heterogeneity of these MLG electrodes. (D) Quantified kinetic values of $C1^{\bullet+}$ (blue points) and $C7^{\bullet+}$ (gold points) reduction at another MLG substrate as a function of substrate overpotential for the redox species. Points represent k_f values for a pixel over the substrate in SECM images, and the width of the distribution shows the relative population of pixels with that value. (E) Quantified kinetic values from $C1^{\bullet+}$ reduction following the data in (A). (F) Quantified kinetic values from $C7^{\bullet+}$ reduction following the data in (B). Green and red lines indicate the limits of quantification for positive and negative feedback, respectively, with our given electrode geometries. k_f values were quantified at substrate open circuit (gray points) and biasing the substrate (red points) at -0.2 V vs. Fc/Fc^+ which is ca. -0.75 V overpotential for the redox couples.

Impact of catholyte chemical structure

Figure 1 shows SECM images of MLG electrodes using C1 and C7 as the catholyte in 0.1 M $LiBF_4$. The MLG electrodes presented a heterogeneous structure with a striped pattern displaying different number of graphitic layers (Figure 1C); the rate of electron transfer has been shown to be sensitive to the layer number,[44] so we used this structure to our advantage as it reveals changes in the heterogeneity of reactive sites at the MLG basal plane. Qualitatively comparing Figures 1A and 1B, it is clear that C1 and C7 exhibit different degrees of reactive heterogeneity on MLG, as C1 reveals more of the underlying substrate structure than C7. However, MLG electrodes of identical structure were used for both catholytes, as shown by SEM, transmittance, and Raman characterization (Figures 1C, S1 and S2). This suggests that C1 and C7 present differences in their electron transfer behavior at the interface. Thus, we turned to determining the distributions of rate constants for ET from the SECM feedback images.

At a given tip-substrate distance, the kinetics of electron transfer in the feedback cycle determine the current at the tip: extremely fast kinetics give a totally mass transport-limited current known as positive feedback (PF), while extremely sluggish kinetics result in a lower limit known as negative feedback (i.e., NF, dominated by hindered mass transport). In contrast, ET limited by the chemistry or electrochemistry at the substrate will give mixed responses and currents in between these two limits. Rate constants in the range of 10^{-6} to 10^{-3} m/s can be confidently quantified using our probe geometry. Inspection of C7 rate constant plots versus overpotential applied at the substrate show that the forward rate constant for ET (k_f) for reduction of tip-generated $C7^{\bullet+}$ at the substrate does not approach the mass transport-limited value (green confidence interval) characteristic of positive feedback. At the overpotentials explored in Figure 1D, the rate constant for ET did not scale as predicted by the Butler-Volmer model with a commonly assumed value for $\alpha \sim 0.5$, as deduced from Eqs. 1 and 2:

(1) $$k_f = k^0 e^{\left(\frac{-\alpha F \eta}{RT}\right)}$$

(2) $$\ln k_f = \ln k^0 - \left(\frac{\alpha F}{RT}\right)\eta$$

Where k_f is the forward rate constant for reducing the oxidized molecule, k^0 is the standard rate constant intrinsic to the redox couple, α is the transmission coefficient, F is Faraday's constant, R is the gas constant, T is the temperature, and η is the applied overpotential, here defined as $\eta = E - E^0$, where E is the electrode potential and E^0 is the standard redox potential of the molecule.

Analysis of the slopes (Eq. 2) using the median value for k_f in Figure 1D shows that the experimental values of α are 0.028 and 0.017 respectively for C1 and C7. For a typical outer-sphere process, one would expect an α of 0.5; at overpotentials past 0.15 V, this would result in higher SECM currents closer to the positive feedback mass transport limit, as has been seen on debris-free graphitic electrodes.[45] For standard redox couples, α in a range of 0.3 to 0.7 has been observed on graphene.[46] However, ET behavior can be variable depending of the number of layers of graphene.[47,48,49] On single layer graphene, SECM showed that redox mediators with finite kinetics ($Ru(NH_3)_6^{3+}$, ferrocenemethanol, etc.) display α values of 0.1 and 0.9, well outside the expected range.[50] In our case, the exceptionally low α values may extend beyond the attenuation

of α from the graphene surface alone. These trends might arise from the presence of a pinhole or porous film,[38,51] the redox species being adsorbed to the electrode,[52] or the presence of a redox-active film mediating ET.[53] This suggests that in the case of C7, and to a lesser extent C1, kinetic control of the rate of ET originates from interfacial structures that are an interplay of the redox active molecule and the graphitic electrode.

Cyclic voltammetry of an MLG electrode cycled in C1 or C7 and tested in blank electrolyte after thorough rinsing showed evidence of a redox-active species remaining at the electrode (Figures S11-S12, S14-S15). While C1 displayed trace amounts of this residual species (which disappeared after cycling), C7 displayed a pronounced CV feature. The voltammetric profile for this feature did not display the typical characteristics of a surface-confined redox species (i.e. no peak-to-peak separation, and a Gaussian profile), but its resilience to rinsing and prolonged cycling, as well as the absence of C7 in solution (as probed through an independent Pt UME placed in the electrolyte) strongly suggest its association with the MLG surface. Multi-layer redox-active films often display diffusional limitations in their charge transfer, leading to similar voltammetric profiles even when surface bound.[54,55] We hypothesize that if a redox-active film is controlling electron transfer rates, then the transfer properties would be determined by the reduced or oxidized population of the film.[56] At the probed potentials, all species based on the DAB core would be in the reduced state, and assuming a uniform surface coverage, a similar rate across the entire electrode regardless of overpotential is expected; this is consistent with Figure 1D and is indeed observed in Figure 1F, where this effect is shown to be highly resilient to cycling. We cannot discard that, in addition to this potential redox-active film, contributions from pinholes in a surface film also play a role in controlling the rate of ET, as this would also give virtually potential-independent k_f values.[38,51] Further support for the presence of a film can be obtained from the distribution of rate constants in Figures 1E and 1F: C1 shows a wider distribution of kinetics, which speaks to the participation of the various surface features inherent to the MLG electrode on the ET process, while C7 is very consistent, suggesting a more homogeneous interface as would be expected for an abundant film covering the electrode.

Cycling the substrate with cyclic voltammetry (CV) perturbs the measured rates from the pristine condition, as seen by the k_f increase from "Initial" to "1 CV" in Figures 1E and 1F and in the SECM images in Figures 1A and 1B. This indicates that some initial thin film forms spontaneously (at least on the order of time of our experiments) and continuously across the electrode when assembled in the cell and solution is added. This initial film is perturbed only once electrochemistry is performed with this substrate electrode, leading to the observed changes in k_f. Further cycling, either through CV or alternating oxidative-reductive potential holds (chronoamperometry, CA) show very little rate drop, which suggests a self-limiting film mechanism if films are forming and controlling rates (Figures 1E and 1F) as opposed to continued growth and passivation. Thus, to see how these films form and under what conditions, we turned to *in situ* AFM.

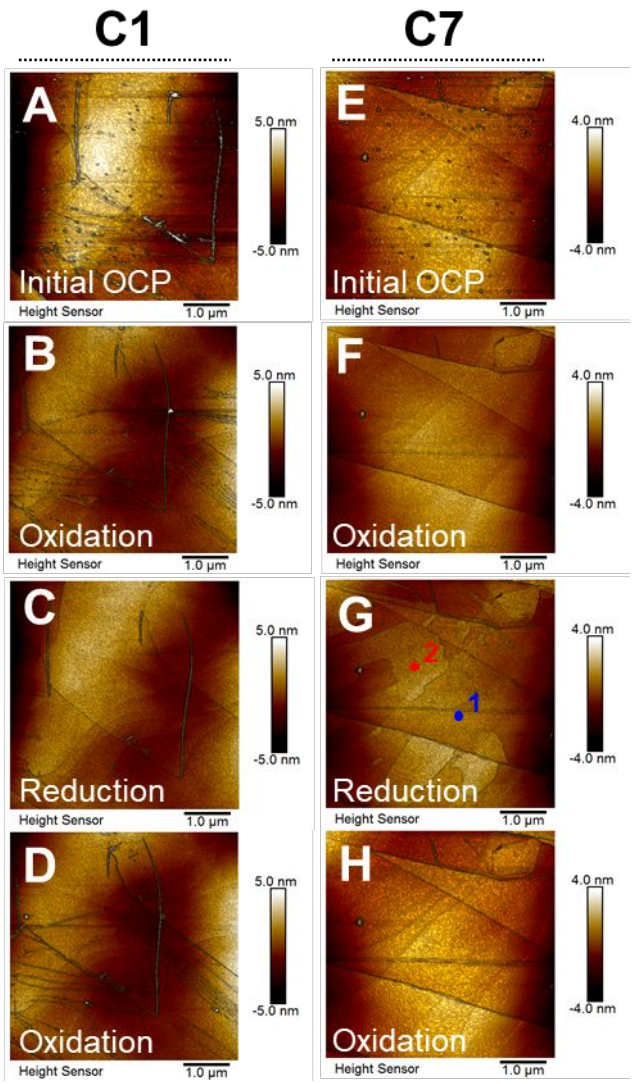

Figure 2. *AFM Imaging of C1 and C7 on HOPG Electrodes*. *In situ* AFM images of the HOPG surface: prior to any electrochemistry at open circuit (Initial OCP), during an anodic potential step (oxidation), during a cathodic potential step (reduction), and a subsequent oxidation step with 5 mM C1 (A-D) and C7 (E-H) catholytes in $LiBF_4$ electrolyte. Points 1 and 2 in (G) refer to unfilmed and filmed HOPG, respectively, as discussed in the text.

AFM of HOPG shows clear basal planes and step edges that are relatively clean before any electrochemistry is performed (Figures 2A and 2E). When oxidizing either C1 or C7, virtually no debris or filming is seen (Figures 2B and 2F). After reducing the radical cations, present in the diffusion layer after an oxidation step, surface products begin to form. In the case of C1 (Figure 2C), some particulate debris forms on step edges. In the case of C7 (Figure 2F), small islands of film, nominally 0.5 nm thick (Figure S18), form on the basal plane and grow the longer the reducing potential is held until reaching the limiting sizes observed in Figure 2G.

To help identify the origin of these films, nanomechanical mapping was employed to determine film properties. Comparison of the maximum force required to remove the silicon nitride cantilever tip from the surface shows that the adhesive force for the film is ~300 pN lower than the graphite

basal plane (Figure S18). Reduced tip-film adhesion relative to graphite could be a result of tip-induced removal of the outer weakly adherent molecular layer. We note that low adhesion forces are reported for polycyclic aromatic hydrocarbons (e.g. 55 pN for pyrene) on the graphite basal plane in aqueous media.[57] We also find that the films are more mechanically compliant as measured from cantilever retraction curves using a DMT-based analysis.[58] A map of effective elastic modulus (Figure S18) yields a discernable, uniform decrease in magnitude for the filmed regions relative to the basal plane. A more mechanically compliant response is reasonable for π-stacked DAB molecules on the basal plane given the absence of extended lateral bonding of aromatic rings. We emphasize that this modulus comparison is qualitative as the limiting thickness of these films (0.5 nm) is below the typical extent of surface deformation (~2 nm) required for quantitative measurements of elastic modulus. Together, these mechanical properties support the notion that an organically derived film builds on the basal planes of graphitic carbon during reductive conditions. Additionally, C1 does not show these basal plane deposits (Figure 2C), indicating that the chemistry of catholyte might determine the surface products. Indeed, as pointed out in Scheme 1, product analysis of bulk electrolysis of related DAB molecules have shown that dimerization processes are observed for sterically unhindered species.[26,27] This is a process that potentially occurs in the diffusion layer at the vicinity of the MLG electrode, although it would likely lead to the formation of a chemically irreversible dimer that may precipitate or adsorb on the electrode surface.

Nonetheless, re-oxidation of the catholyte quickly refreshes the electrode surface, with most films and edge deposits disappearing in subsequent AFM images (Figures 2D and 2H). The application of a potential bias may electrostatically desorb these films, but it is also possible that these potentials change the redox state of the films (i.e., neutral to positively charged) and thus increase their solubility. This result indicates that interfacial reactivity is mostly reversible and helps explain why little passivation is seen over the course of SECM experiments while cycling the electrodes. We note that the SECM experiments are always performed under conditions where the oxidized products of C1 and C7 are generated above the MLG plane, so any mechanisms resulting from radical cation reactions would be operating during all experiments and the consequences apparent in all results. The adsorption of the reduced form of a redox couple inhibiting electron transfer to the oxidized form on carbon surfaces has been observed for cobalt phenanthroline complexes;[59] it is likely that a similar phenomenon with C7 or C7-based products is taking place here.

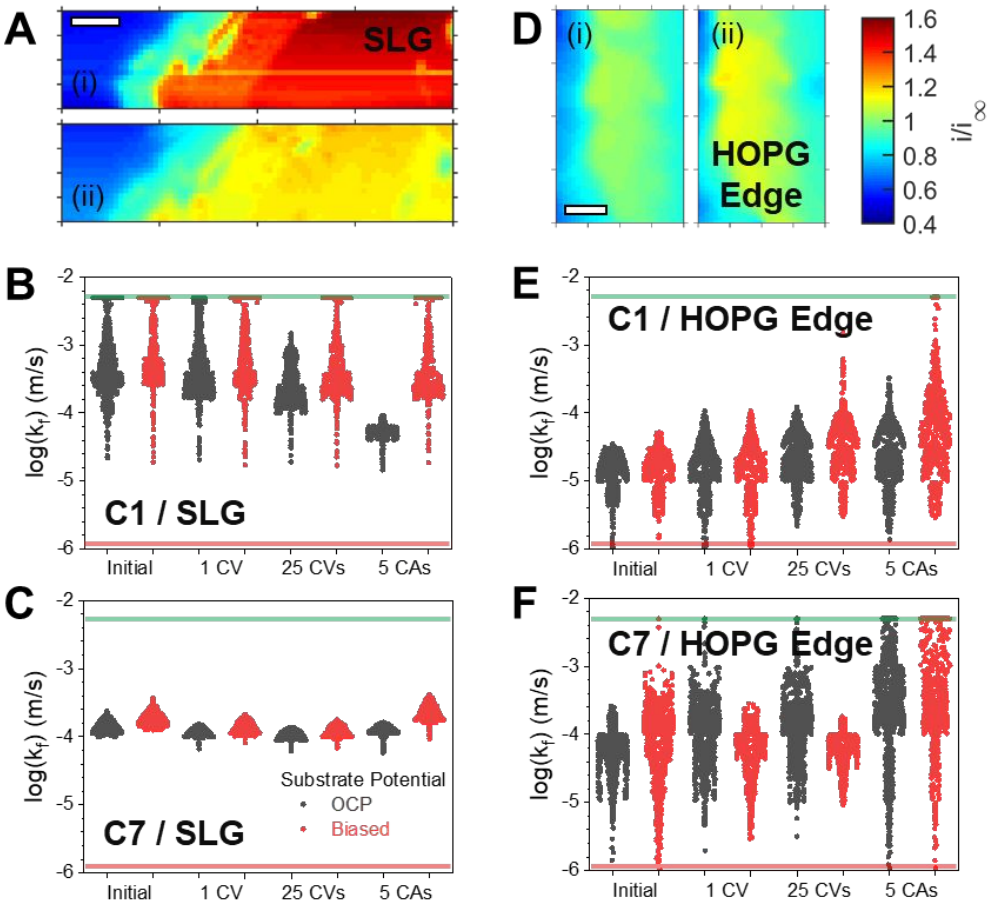

Figure 3. *Comparison of SLG and HOPG Edge Electrodes*. Normalized SECM images with 5 mM C1 catholyte mediator in $LiBF_4$ electrolyte on (A) SLG and (D) HOPG edge substrates at open circuit. Image scale bars are 20 μm; images were taken (i) at the initial condition before substrate biasing and (ii) after 26 substrate CVs and 5 CAs. Quantified kinetic values for $C1^{+\bullet}$ reduction on (B) SLG and (E) HOPG edge electrodes at OCP (gray points) and biased at -0.2 V for SLG and 0.0 V for HOPG edge (red points). Quantified kinetic values for $C7^{+\bullet}$ reduction on (C) SLG and (F) HOPG edge electrodes at OCP (gray points) and biased at -0.2 V for SLG and -0.3 V for HOPG edge (red points). Green and red lines indicate the limits of quantification for positive and negative feedback, respectively, with our given electrode geometries.

Impact of electrode structure

AFM images showed different surface structures at step edges and basal planes. To determine the impact of these electrode structures on catholyte reactivity, we "deconstructed" multilayer graphitic carbon to pure basal plane (SLG) and edge plane (HOPG edge) electrodes.

Extended cycling of C1 on SLG shows a distinct lowering of feedback current at substrate open circuit, corresponding to an order of magnitude drop in median k_f values (Figures 3A and 3B). The distribution of k_f values also shrinks, suggesting a film has formed that controls the electron transfer rate as in the case of C7 on MLG (Figure 1F). Figures 3B and 3C for C1 and C7 on SLG show a slight improvement in kinetics when biasing the electrode at -0.2 V vs. the case for OCP, consistent with the reversible reactivity of these filmed interfaces and the redox

mediating role of the films. This result highlights the power of open circuit feedback imaging, where subtle changes in reactivity in biased imaging are exacerbated at open circuit due to the mechanism of electron shuttling.[38,42]

C7 kinetics on SLG decrease slightly with cumulative redox cycling, but not nearly as much as C1. The C7-SLG behavior is more similar to MLG, indicating that the C7-based film is more ubiquitous on basal planes than C1. We speculate a C1-based film requires the more reactive surface of SLG on SiO_2 to form, as the underlying support greatly influences the electronic properties of SLG electrodes,[24,60] or through the natural corrugation of SLG surfaces.[46]

HOPG edge electrodes with the prismatic planes of HOPG exposed to solution show relatively slow kinetics and wide distributions with both catholytes (Figures 3D-F). These attributes likely result from the uneven nature of the sample, which complicates the fitting procedure (Figure S5). Nonetheless, no passivation is seen for C1 or C7 on HOPG edges; if anything, the feedback current actually increases over time. This indicates that little to no decomposition and byproduct accumulation takes place at step edges and is inconsequential for electron transfer. This is a surprising finding, since edges have higher surface energy compared to basal planes[61] and would be expected to affect more decomposition; HOPG step edges have been known to show increased redox mediator activity.[62] From this, we infer that the films discussed above form on basal panes aided by π–π interactions,[63,64,65] coming from the catholyte or catholyte-derived species, which is plausible given the structure of C1 and C7.

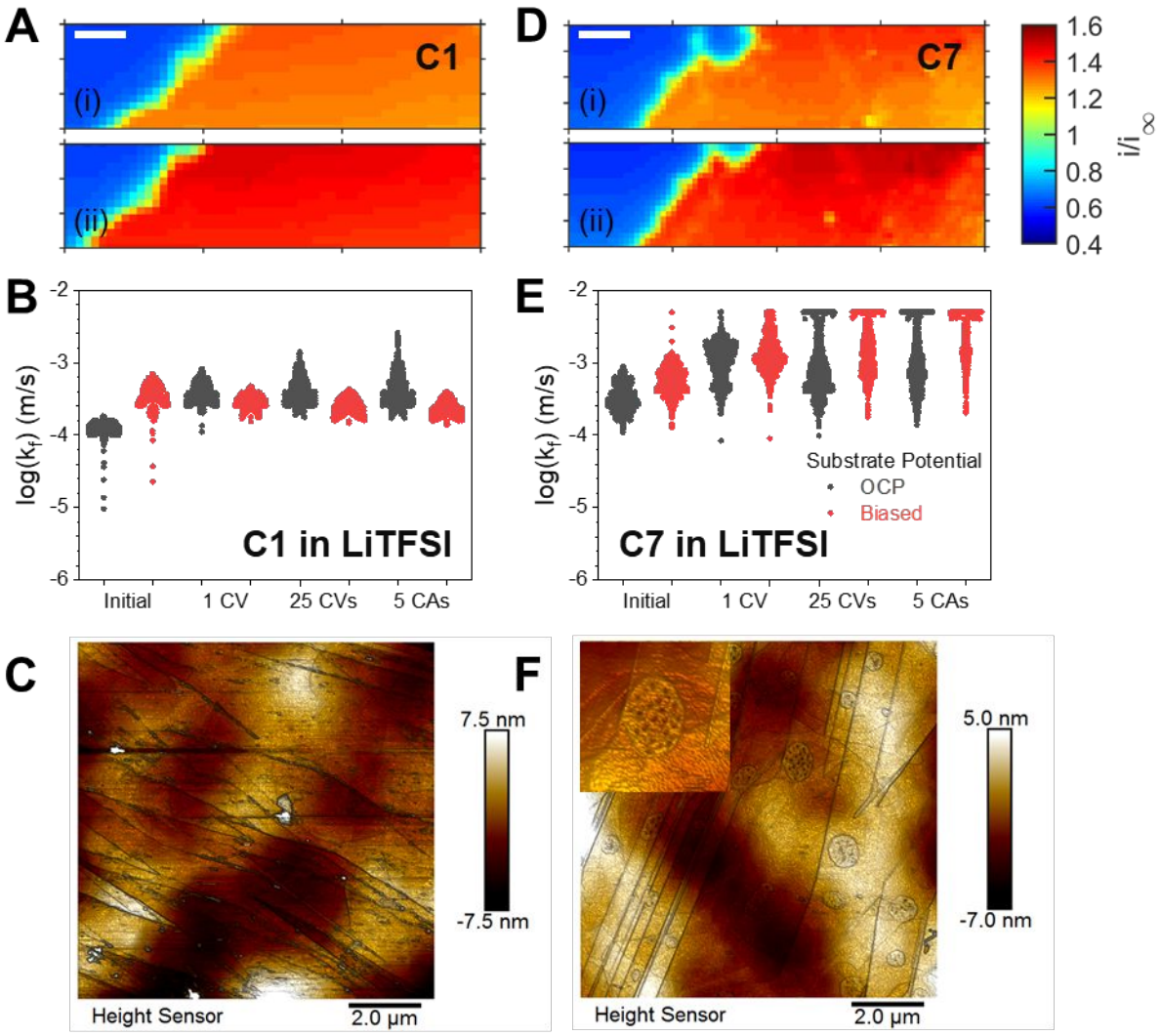

Figure 4. *Comparing Behavior with LiTFSI Electrolyte*. Normalized SECM images of MLG substrates at open circuit with 5 mM (A) C1 and (D) C7 catholyte mediators in 0.1 M LiTFSI electrolyte. Image scale bars are 20 µm; images were taken (i) at the initial condition before substrate biasing and (ii) after 26 substrate CVs and 5 CAs. Quantified kinetic values for (E) $C1^{+\bullet}$ and (F) $C7^{+\bullet}$ reduction at OCP (gray points) and biased (red points) at -0.5 V for C1 and -0.1 V for C7. Green and red lines indicate the limits of quantification for positive and negative feedback, respectively, with our given electrode geometries. *In situ* AFM images of HOPG electrodes with (C) C1 and (F) C7 catholytes in LiTFSI electrolyte following reductive holds to reduce oxidized catholyte. Inset shows a magnified image of a filmed region displaying a porous structure.

Impact of electrolyte composition

We next wanted to understand if these film-forming mechanisms are generalized across electrolytes given the testing conditions used here with C1 and C7 catholytes. Electrolyte effects may impact the solubility and adsorption properties of the radical cations and any newly formed species. In addition, different mechanisms at highly polarized electrodes could take place due to differences in the structure of the double layer. We compared $LiBF_4$ and LiTFSI electrolytes to determine if and how anions impact catholyte stability at the interface.

For C1 in LiTFSI, similar long-term trends are seen as with C1 on MLG with $LiBF_4$ electrolyte, where an initial increase in kinetics at OCP levels off after CV and CA cycles (Figures 4A and 4B). However, no striations with different kinetic values are seen in the images, and the k_f distributions are smaller, indicating that a film is obscuring the heterogeneity of the substrate seen in the case of C1-MLG-$LiBF_4$ (Figure 1A). Additionally, biasing the electrode at reducing potentials actually slightly decreases the kinetic values during imaging (Figure 4B). This may indicate that reduction of catholyte radical species in the presence of $TFSI^-$ causes active film formation that hinders electron transfer, though again the film dissipates after cycling (Figure S27).

An opposite trend is seen for C7-MLG-LiTFSI (Figures 4D and 4E), where striations now appear and kinetics are faster and more distributed compared to the $LiBF_4$ electrolyte (Figure 1B). Perhaps in LiTFSI, C7-based films are less stable or less favorable to form and thus do not uniformly cover the electrode, exposing its heterogeneity. AFM images (Figure 4F) show that C7 cycling in LiTFSI still forms films on the basal plane, but the films are more porous than those in $LiBF_4$. More porous films in conjunction with a return of substrate heterogeneity in SECM lends credence to one of our hypotheses about pinhole films controlling the kinetics of electron transfer in the C7 catholyte system. C1 in LiTFSI electrolyte shows substantially more debris forming than in $LiBF_4$, though no films form like in the case of C7 (Figure 4C). This debris, if insulating, would act in much the same way as a pinhole film where electrode sites are blocked, thus limiting overall feedback. Overall, however, both $LiBF_4$ and LiTFSI seem to be compatible with both C1 and C7 catholytes, since no catastrophic irreversible passivation is seen on this scale of redox activity. LiTFSI has actually been shown to be an optimal (co-)salt for C1 as it enables better solubility and conductivity.[33]

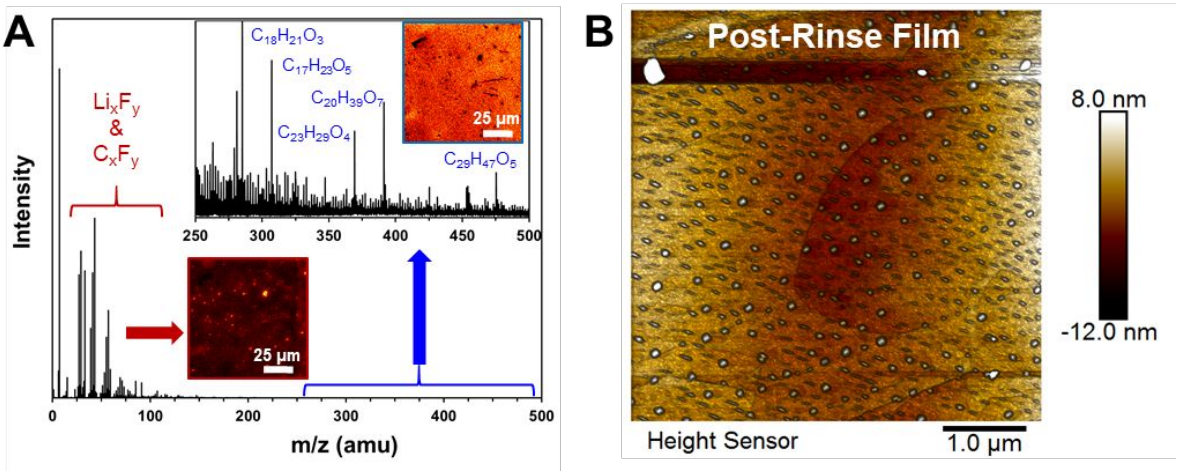

Figure 5. *Post-Cycling SIMS Analysis of Decomposition Products*. (A) ToF-SIMS positive ion spectra and composition maps of an HOPG surface sample after cycling in a C7-$LiBF_4$-PC electrolyte (monomer $C_{10}H_{14}O_2H^+$, 167 amu; dimer $C_{20}H_{26}O_4H^+$, 331 amu). Li_xF_y and C_xF_y species and larger organic species are prevalent as indicated by secondary ion generation in the low and high mass regions of the spectrum, respectively. Compositional maps (inset) show the organic components uniformly distributed across the surface with isolated regions of high inorganic content. (B)) Post-rinse ex situ AFM image of same C7-derived film analyzed via SIMS.

Finally, to determine the chemical makeup of these surface decomposition products, we employed SIMS *ex situ* on HOPG samples cycled in C7 (Figure 5). While the composition of the

filmed electrode is complex and no distinct organic polymeric species can be distinguished (e.g, the C7 dimer, Scheme 1), both inorganic and organic compounds were detected. The higher mass ions could indicate polymerization reactions involving the PC solvent with itself or between the solvent and the catholyte. An active role of the electrolyte is consistent with the formation of C-F and Li-F species indicating electrolyte decomposition is taking place. Since both the redox species and solvent contain C-O species, it is difficult to tell if solvent decomposition or catholyte decomposition originate the species detected at high *m*/*z* ratios (Figure 5A, inset).

Additionally, these chemistries can be heterogeneous across the electrode, as shown in the mapping of inorganic vs. organic products on this sample (Figure 5A, inset images). It appears that small inorganic particulates are embedded in a more homogeneous organic film. It remains unclear how much of the generated surface products are retained after the careful rinsing procedure, but these preliminary experiments are a promising first step for understanding the chemical mechanisms underlying structural evolution of the interface. We are currently developing *in situ* spectroelectrochemical systems to identify specific product chemistries and directly correlate electrode structure (i.e., graphene layer number, defect density) with local electrochemical activity.[66]

Conclusions

We established a methodology using the advantages of both SECM and AFM to interrogate the impact of interfacial processes on electron transfer for a model catholyte in NRFBs. SECM enabled the quantification of ET kinetics as well as the heterogeneity in electrode behavior, suggesting reactivity differences for similar dialkoxybenzene molecules C1 and C7. In most cases, but certainly at the basal plane of MLG and SLG, C1 and C7 failed to reach mass-transfer limited reactivity at high overpotential for reduction of the corresponding radical cations, suggesting the formation of interfacial structures which controlled the reaction kinetics. AFM confirmed the formation of surface films with distinct mechanical properties; these films formed conditionally on electrodes and were correlated to the reactive changes observed in SECM experiments. Voltammetric analysis revealed that these films are redox-active, although their kinetic stability towards desorption on the MLG surface differs, with that formed with C7 being more persistent. SIMS analysis on these films showed they contain both organic and inorganic components, suggesting the participation of the supporting electrolyte in the film formation process, although the mechanisms of formation seem complex. We further observed that electron transfer on the edge plane was relatively insensitive to the formation of these surface products, while monolayer graphene exhibited more pronounced decreases in reactivity as the electrode was cycled. These rate-limiting films seem to affect primarily the basal plane of graphitic carbons, a likely indication of π–π interactions, thus suggesting new directions in the fabrication or treatment of electrodes with better resilience against these unwanted processes. Altogether, this integrated methodology opens new opportunities in the characterization of redox processes for RFBs, including aqueous and non-aqueous systems, where interfacial processes associated with adsorption and film formation may become dominating at high active concentrations.

Conflicts of Interest

The authors declare no conflicts of interest.

Acknowledgments

This research was financially supported by the Joint Center for Energy Storage Research (JCESR), an Energy Innovation Hub funded by the U.S. Department of Energy, Office of Science, and Basic Energy Sciences. Sandia National Laboratories is a multimission laboratory managed and operated by National Technology & Engineering Solutions of Sandia, LLC, a wholly owned subsidiary of Honeywell International Inc., for the U.S. Department of Energy's National Nuclear Security Administration under contract DE-NA0003525. The submitted manuscript has also been created by UChicago Argonne, LLC, Operator of Argonne National Laboratory ("Argonne"). Argonne, a U.S. Department of Energy Office of Science laboratory, is operated under Contract No. DE-AC02-06CH11357. Materials characterization was carried out in part in the Material Research Laboratory Central Facilities and at the Beckman Institute for Advanced Science and Technology at the University of Illinois at Urbana-Champaign. D.S. thanks Yana Zhou for assistance with optical profilometry and Kendrich Hatfield for assistance with DigiElch modelling. K.Z. thanks James A. Ohlhausen for assistance with ToF-SIMS analysis. J.R-L. acknowledges the Alfred P. Sloan Foundation Fellowship.

References

[1] Z. Yang, J. Zhang, M. C. W. Kintner-Meyer, X. Lu, D. Choi, J. P. Lemmon and J. Liu, *Chem. Rev.*, 2011, **111**, 3577–3613.
[2] Y. Zhen, C. Zhang, J. Yuan, Y. Zhao and Y. Li, *J. Power Sources,* 2020, **445**, 227331.
[3] A.Z. Weber, M.M. Mench, J.P. Meyers, P.N. Ross, J.T. Gostick and Q. Liu, *J. Appl. Electrochem.*, 2011, **41**, 1137-1164.
[4] M.H. Chakrabarti, N.P. Brandon, S.A. Hajimolana, F. Tariq, V. Yufit, M.A. Hashim, M.A. Hussain, C.T.J. Low and P.V. Aravind, *J. Power Sources*, 2014, **253**, 150-166.
[5] S. Ha and K.G. Gallagher, *J. Power Sources*, 2015, **296**, 122-132.
[6] K.J. Kim, M.-S. Park, Y.-J. Kim, J.H. Kim, S.X Dou and M. Skyllas-Kazacos, *J. Mater. Chem. A*, 2015, **3**, 16913-16933.
[7] N. Roznyatovskaya, J. Noack, K. Pinkwart and J. Tübke, *Curr. Opin. Electrochem.*, 2020, **19**, 42-48.
[8] M. Burgess, K. Hernández-Burgos, J.K. Schuh, J. Davila, E.C. Montoto, R.H. Ewoldt and J. Rodríguez-López, *J. Am. Chem. Soc.*, 2018, **140**, 2093-2104.
[9] M.-A. Goulet, L. Tong, D.A. Pollack, D.P. Tabor, S.A. Odom, A. Aspuru-Guzik, E.E. Kwan, R.G. Gordon and M.J. Aziz, *J. Am. Chem. Soc.*, 2019, **141**, 8014-8019.
[10] C.S. Sevov, D.P. Hickey, M.E. Cook, S.G. Robinson, S. Barnett, S.D. Minteer, M.S. Sigman and M.S. Sanford, *J. Am. Chem. Soc.*, 2017, **139**, 2924-2927.
[11] Y. Yan, S.G. Robinson, M.S. Sigman and M.S. Sanford, *J. Am. Chem. Soc.*, 2019, **141**, 15301-15306.
[12] Y. Ding, C. Zhang, L. Zhang, Y. Zhou and G. Yu, *Chem*, 2019, **5**, 1964-1987.
[13] J. Luo, B. Hu, M. Hu, Y. Zhao and T.L. Liu, *ACS Energy Lett.*, 2019, **4**, 2220-2240.
[14] M. Burgess, J.S. Moore and J. Rodríguez-López, *Acc. Chem. Res.*, 2016, **49**, 2649-2657.

[15] M.J. Baran, M.N. Braten, E.C. Montoto, Z.T. Gossage, L. Ma, E. Chénard, J.S. Moore, J.S., Rodríguez-López and B.A. Helms, *Chem. Mater.*, 2018, **30**, 3861-3866.
[16] Y.G. Zhu, Y. Du, C. Jia, M. Zhou, L. Fan, X. Wang and Q. Wang, *J. Am. Chem. Soc.*, 2017, **139**, 6286-6289.
[17] X. Wei, W. Xu, M. Vijayakumar, L. Cosimbescu, T. Liu, V. Sprenkle and W. Wang, *Adv. Mater.*, 2014, **26**, 7649–7653.
[18] M. O. Bamgbopa, Y. Shao-Horn and S. Almheiri, *J. Mater. Chem. A*, 2017, **5**, 13457–13468.
[19] S.-H. Shin, S.-H. Yun and S.-H. Moon, *RSC Adv.*, 2013, **3**, 9095–9116.
[20] E.V. Carino, D.J. Newman, J.G. Connell, C. Kim and F.R. Brushett, *Langmuir*, 2017, **33**, 11911-11918.
[21] K. Wedege, E. Dražević, D. Konya and A. Bentien, *Sci. Rep.*, 2016, **6**, 39101.
[22] X. Wei, W. Xu, J. Huang, L. Zhang, E. Walter, C. Lawrence, M. Vijayakumar, W.A. Henderson, T. Liu, B. Li, V. Sprenkle and W. Wang, *Angew. Chem.*, 2015, **54**, 8684-8687.
[23] J.A. Mann, J. Rodríguez-López, H.D. Abruña and W.D. Dichtel, *J. Am. Chem. Soc.*, 2011, **133**, 17614-17617.
[24] J. Hui, S. Pakhira, R. Bhargava, Z.J. Barton, X. Zhou, A.J. Chinderle, J.L. Mendoza-Cortes and J. Rodríguez-López, *ACS Nano*, 2018, **12**, 2980-2990.
[25] J.A. Kowalski, L. Su, J.D. Milshtein and F.R. Brushett, *Curr. Opin. Chem. Eng.*, 2016, **13**, 45-52.
[26] J. Huang, B. Pan, W. Duan, X. Wei, R. S. Assary, L. Su, F. R. Brushett, L. Cheng, C. Liao, M. S. Ferrandon, W. Wang, Z. Zhang, A. K. Burrell, L. A. Curtiss, I. A. Shkrob, J. S. Moore and L. Zhang, *Sci. Rep.* 2016, **6**, 32102.
[27] J. Huang, L. Su, J. A. Kowalski, J. L. Barton, M. Ferrandon, A. K. Burrell, F. R. Brushett and L. Zhang, *J. Mater. Chem. A*, 2015, **3**, 14971–14976.
[28] H. Bülter, F. Peters, J. Schwenzel and G. Wittstock, *Angew. Chem.*, 2014, **53**, 10531-10535.
[29] H. Bülter, M. Sternad, E. dos Santos Sardinha, J. Witt, C. Dosche, M. Wilkening and G. Wittstock, *J. Electrochem. Soc.*, 2016, **163**, A504-A512.
[30] H. Bülter, P. Schwager, D. Fenske and G. Wittstock, *Electrochim. Acta*, 2016, **199**, 366-379.
[31] G. Zampardi, R. Trocoli, W. Schuhmann and F. La Mantia, *Phys. Chem. Chem. Phys.*, 2017, **19**, 28381-28387.
[32] G. Zampardi, F. La Mantia and W. Schuhmann, *RSC Adv.*, 2015, **5**, 31166-31171.
[33] L. Su, M. Ferrandon, J.A. Kowalski, J.T. Vaughey and F.R. Brushett, *J. Electrochem. Soc.*, 2014, **161**, A1905-A1914.
[34] P.R. Unwin, A.G. Güell and G. Zhang, *Acc. Chem. Res.*, 2019, **49**, 2041-2048.
[35] C.E. Banks, T.J. Davies, G.G. Wildgoose and R.G. Compton, *Chem. Commun.*, 2005, 829-841.
[36] C.E. Banks and R.G. Compton, *Analyst*, 2006, **131**, 15-21.
[37] Z.T. Gossage, J. Hui, Y. Zeng, H. Flores-Zuleta and J. Rodríguez-López, *Chem. Sci*., 2019, 10, 10749-10754.
[38] C. Lefrou and R. Cornut, *ChemPhysChem*, 2010, **11**, 547-556.
[39] H. Xiong, J. Guo and S. Amemiya, *Anal. Chem.*, 2007, **79**, 2735-2744.
[40] H. Xiong, J. Kim, E. Kim and S. Amemiya, *J. Eelectroanal. Chem.*, 2009, **629**, 78-86.
[41] H. Bülter, F. Peters, J. Schwenzel and G. Wittstock, *ECS Trans.*, 2015, **66**, 69-79.
[42] A.I. Oleinick, D. Battistel, S. Daniele, I. Svir and C. Amatore, *Anal. Chem.*, 2011, **83**, 4887-4893.
[43] J.A. Olhausen and K.R. Zavadil, *J. Vac. Sci. Technol. A*, 2006, **24**, 1172-1178.
[44] A.G. Güell, N. Ebejer, M.E. Snowden, J.V. Macpherson and P.R. Unwin, *J. Am. Chem. Soc.*, 2012, **134**, 7258-7261.
[45] S. Amemiya, R. Chen, N. Nioradze and J. Kim, *Acc. Chem. Res.*, 2016, **49**, 2007-2014.
[46] W. Li, C. Tan, M.A. Lowe, H.D. Abruña and D.C. Ralph, *ACS Nano*, 2011, **5**, 2264-2270.
[47] A.T. Valota, I.A. Kinloch, K.S. Novoselov, C. Casiraghi, A. Eckmann, E.W. Hill and R.A.W. Dryfe, *ACS Nano*, 2011, **5**, 8809-8815.
[48] A.T. Valota, P.S. Toth, Y.-J. Kim, B.H. Hong, I.A. Kinloch, K.S. Novoselov, E.A. Hill and R.A.W. Dryfe, *Electrochim. Acta*, 2013, **110**, 9-15.
[49] M. Velický, D.F. Bradley, A.J. Cooper, E.W. Hill, I.A. Kinloch, A. Mishchenko, K.S. Novoselov, H.V. Patten, P.S. Toth, A.T. Valota, S.D. Worrall and R.A.W. Dryfe, *ACS Nano*, 2014, **8**, 10089-10100.
[50] N.L. Ritzert, J. Rodríguez-López, C. Tan and H.D. Abruña, *Langmuir*, 2013, **29**, 1683-1684.
[51] A. Kiani, M.A. Alpuche-Aviles, P.K. Eggers, M. Jones, J.J. Gooding, M.N. Paddon-Row and A.J. Bard, *Langmuir*, 2008, **24**, 2841-2849.
[52] R. Guidelli, R.G. Compton, J.M. Feliu, E. Gileadi, J. Lipkowski, W. Schmickler and S. Trasatti, *Pure Appl. Chem.*, 2014, **86**, 259-262.
[53] M. Tsionsky and A.J. Bard, *Chem. Mater.*, 1998, **10**, 2120-2126.
[54] T. Ikeda, C.R. Leidner and R.W. Murray, *J. Electroanal. Chem. Interfacial Electrochem.*, 1982, **183**, 343-365.
[55] M.E.G. Lyons, *Electroactive Polymer Electrochemistry*, Spring-Verlag US, Boston, 1994.
[56] R.H. Schmehl and R.W. Murray, *J. Electroanal. Chem. Interfacial Electrochem.*, 1983, **152**, 97-109.

[57] Y. Zhang, C. Liu, W. Shi, Z. Wang, L. Dai and X. Zhang, *Langmuir*, 2007, **23**, 7911-7915.
[58] B.V. Derjaguin, V.M. Muller and Y.P. Toporov, *Prog. Surf. Sci.*, 1994, **45**, 131-143.
[59] R. Chen, A. Morteza Najarian, N. Kurapati, R.J. Balla, A. Oleinick, I. Svir, C. Amatore, R.L. McCreery and S. Amemiya, *Anal. Chem.*, 2018, **90**, 11115-11123.
[60] J. Hui, S. Pakhira, R. Bhargava, Z.J. Barton, X. Zhou, A.J. Chinderle, J.L. Mendoza-Cortes and J. Rodríguez-López, *ACS Nano*, 2018, **12**, 2980-2990.
[61] J. Abrahamson, *Carbon*, 1973, **11**, 337-362.
[62] A.G. Güell, A.S. Cuharuc, Y.-R. Kim, G. Zhang, S. Tan, N. Ebejer and P.R. Unwin, *ACS Nano*, 2015, **9**, 3558-3571.
[63] N. Kirupati, P. Pathirathna, R. Chen and S. Amemiya, *Anal. Chem.*, 2018, **90**, 13632-13639.
[64] G. Zhang, P.M. Kirkman, A.N. Patel, A.S. Cuharuc, K. McKelvey and P.R. Unwin, *J. Am. Chem. Soc.*, 2014, **136**, 11444-11451.
[65] J. Xu, Q. Chen and G.M. Swain, *Anal. Chem.*, 1998, **70**, 3146-3154.
[66] N.B. Schorr, A.G. Jiang and J. Rodríguez-López, *Anal. Chem.*, 2018, **90**, 7848-7854.

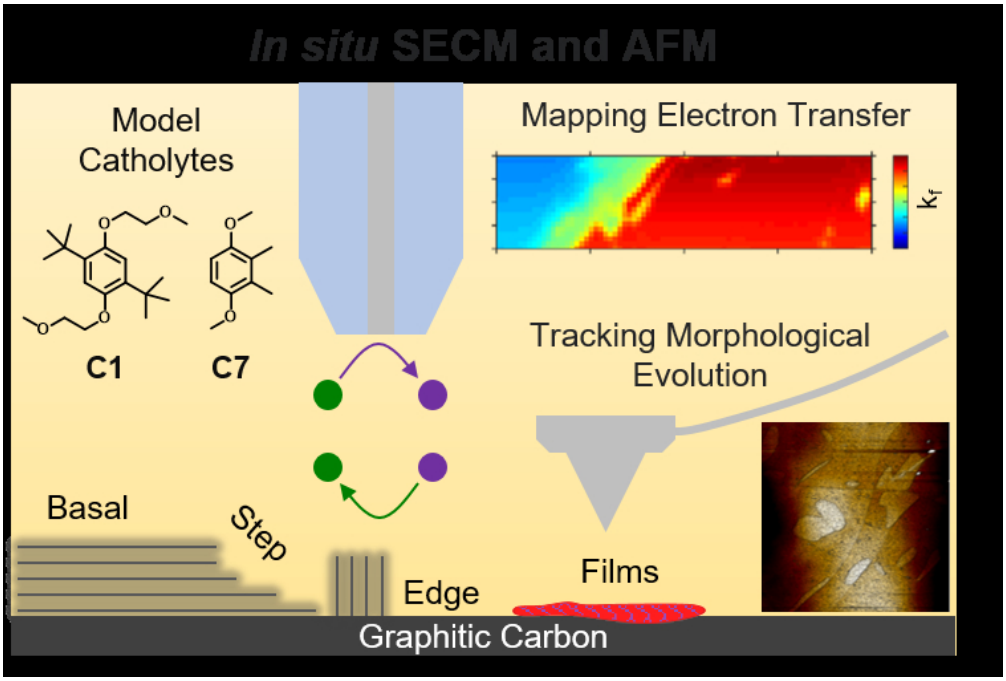
In situ SECM and AFM
Model Catholytes
C1
C7
Mapping Electron Transfer
k_f
Tracking Morphological Evolution
Basal
Step
Edge
Films
Graphitic Carbon